RESEARCH ARTICLE

Zeolite Y-supported carbon-doped TiO$_2$ nanocomposites: Efficient solar photocatalysts for the purification of medicinal wastewater

Mekha Susan Rajan[1] · Anju John[1] · Minjoong Yoon[2] · Jesty Thomas[1]

Abstract

The existence of antibiotics in aquatic streams destroys water quality and thereby poses serious ecological hitches. Photocatalysis involving nanosemiconductors is an environmentally benign technique for the mineralization of antibiotics. Herein, we prepared a new visible light–sensitive photocatalyst, zeolite Y-supported carbon-doped TiO$_2$ nanocomposite (zeolite Y-c-TiO$_2$), for the elimination of cefazolin antibiotic in wastewater systems. The structural and optical properties of the synthesized nanocomposites were investigated by Fourier transform infrared spectroscopy (FT-IR), powder X-ray diffraction analysis (XRD), scanning electron microscopy (SEM), energy-dispersive X-ray analysis (EDX), transmission electron microscopy (TEM), X-ray photoelectron spectroscopy (XPS), and Brunauer-Emmett-Teller surface area analysis (BET) as well as diffuse reflectance spectroscopy (UV-DRS) and photoluminescence spectroscopy (PL). The UV-Vis absorbance spectrum of zeolite Y-c-TiO$_2$ exhibited a red shift towards longer wavelength with an increase in visible light absorption as compared to pure TiO$_2$ nanoparticles and zeolite Y-supported TiO$_2$ nanocomposites (zeolite Y-TiO$_2$). Accordingly, the photocatalytic action of the zeolite Y-c-TiO$_2$ for the degradation of methylene blue was evaluated under solar simulator, and it turned out to be highly efficient (100%) mineralization as compared to TiO$_2$-nanoparticles (42%) and zeolite Y-TiO$_2$ (62%) after 70 min irradiation for a 50mg L^{-1} methylene blue solution. Radical scavenging experiments revealed the involvement of hydroxyl radicals, superoxide radicals, and photogenerated holes in the degradation process. Consequently, zeolite Y-c-TiO$_2$ was applied for the photocatalytic degradation of the cefazolin antibiotic in water, and complete degradation of cefazolin (50 mg L^{-1}) was observed within 6 h of solar light irradiation on zeolite Y-c-TiO$_2$. The degradation pathway of cefazolin was proposed by considering various intermediates detected via LC-MS analysis. The study points to the significant potential of zeolite Y-c-TiO$_2$ photocatalyst for the purification of medicinal wastewater under sunlight.

Keywords Zeolite Y-c-TiO$_2$ nanocomposites · Solar photocatalysis · Dyes · Medicine · Wastewater purification

Introduction

Nowadays, excessive usage of antibiotics and their disposal to the aquatic environment exert undesirable influences on all living systems (Polianciuc et al. 2020). About 50–70% of the entire antibiotics used by human beings come under the group of cephalosporins, which contains beta lactam moiety

Responsible Editor: Sami Rtimi

✉ Jesty Thomas
jestyk@kecollege.ac.in

[1] Research Department of Chemistry, Kuriakose Elias College, Mannanam, Kottayam, Kerala 686561, India

[2] Department of Chemistry, Chungnam National University, Daejeon 34134, Republic of Korea

(Das et al. 2019). The first-generation cephalosporin antibiotic, cefazolin, which is widely used for bacterial disinfection, leads to the generation of antibiotic resistant pathogens when it gets discharged into the environment (Das et al. 2019; Mutuku et al. 2022). Hence, its removal from aquatic streams requires great attention (Das et al. 2019; Iskender et al. 2007). Conventional removal of antibiotics from water used to be managed by ozonation, chlorination, electrochemical oxidation, potassium permanganate, and sulfate radical anion oxidation (Iskender et al. 2007; Chen et al. 2021) or adsorption by clay and activated carbon (Das et al. 2019). However, these methods are found to be less efficient and cost ineffective. In this context, photocatalysis becomes one of the most attractive advanced oxidation processes (AOPs) for the degradation of organic pollutants in water (Davies et al. 2021; Elmolla and Chaudhuri 2010).

Among various photocatalysts, TiO_2 nanoparticles have been the most popular because of their high catalytic efficiency, low cost, as well as eco-friendly behavior with their chemical and thermal stabilities (Rajan et al. 2022a; Pawar et al. 2018). Nevertheless, they have drawbacks such as wide band gap (3.2 eV) to absorb UV light, which limits in using solar light of which visible light provides 42.3% radiation in contrast to 8.2% UV (Rajan et al. 2022a; Van et al. 2022; López-Ortiz et al. 2021). In fact, solar photocatalysis to detoxify the contaminated antibiotics in water resources has become attractive because solar irradiation is saving energy and improves the performance of the AOP technology. TiO_2 nanomaterials which are active under visible light have been developed by doping metals such as Fe, V, Cr, and Tm (Ali et al. 2017; Rossi et al. 2021; Wang et al. 2012; Mazierski et al. 2019) or non-metals such as N and C (Gurkan et al. 2012; Pandi et al. 2022) into the lattices of the TiO_2 nanocrystals. Doping leads to the declination of band gap and also slows down the electron-hole recombination rate which could enhance the photocatalytic activity (Amran et al. 2019). Some of these photocatalysts have been applied to the degradation of antibiotics in water under visible light or solar light irradiation (Gurkan et al. 2012; Pandi et al. 2022). However, they have absorption in the narrow visible region, leading to low photocatalytic efficiency under visible light, and they still leave room for improvement in the optical properties. In addition, surface areas of these TiO_2 nanomaterials themselves are limited in enhancing adsorption of pollutants to increase the catalytic reaction sites. Thus, TiO_2 nanoparticles require hybridization with some support materials of large surface area to enhance the adsorption of pollutants. The common support materials for this purpose are clays (Zhou et al. 2022; Rajan et al. 2022b), mesoporous materials (Vanichvattanadecha et al. 2021), and zeolites (Abbas et al. 2020; Saqib et al. 2019).

Particularly, zeolites are the most attractive support materials due to their unique physicochemical/adsorption properties for catalytic efficiency (Saqib et al. 2019; Payra and Dutta 2003). Various zeolites including zeolites L, Y, and ZSM-5 are crystalline aluminosilicates forming microporous framework enclosing uniform cages and channels of molecular/nanoscales, which provide a novel environment for photo-chemical reactions of molecules and nanoparticles as well as large surface area to adsorb pollutants well enough to increase the surface catalytic sites. Furthermore, it is interesting that muti-electron/hole transfer can take place within and at the interfaces of zeolites (Yoon et al. 2007; Dutta and Severance 2011) to control exciton recombination from the semiconductor photocatalysts. The issues associated with the aggregation of TiO_2 nanoparticles could be cracked by incorporating TiO_2 clusters inside the microporous structure of zeolites (Aprile et al. 2008). In this logic, numerous research works

addressing the photocatalytic applications of TiO_2-zeolites can be observed (Saqib et al. 2019). Liu et al. (2018) studied the degradation of antibiotic, sulfadiazine, by developing a composite photocatalytic material based on natural zeolite coated with TiO_2 synthesized through sol-gel method. The results showed that photodegradation response of sulfadiazine using TiO_2/zeolite photocatalyst is due to the synergistic effect of zeolite adsorbent and TiO_2 photocatalyst. The catalyst could remove 90% of sulfadiazine within 120 min of UV light irradiation. However, this catalyst is not sensitive to visible light. Thus, the visible light–sensitive Fe^{3+} or Fe_2O_3-incorporated zeolite-supported TiO_2 was developed and successfully applied for the degradation of tetracycline and ciprofloxacin under the visible LED light irradiation (Jalloul et al. 2022; Liu et al. 2017). Nevertheless, using metals in the zeolite supported TiO_2 may not be eco-friendly, and hybridization of C or N-doped TiO_2 with zeolite would be highly desirable for the visible light– or solar light–sensitive photocatalysts. Numerous works have been published on the photocatalytic applications of C- or N-doped TiO_2 for the degradation of refractory pollutants (Oseghe and Ofomaja 2018; Xu et al. 2018; Shao et al. 2017; He et al. 2013; Navarra et al. 2022), but carbon-doped TiO_2 supported by zeolites has not been studied yet especially for the solar catalytic degradation of medicinal wastewater.

In this work, in order to develop solar photocatalytic purification technique of medicinal wastewater, we synthesized zeolite Y-supported carbon-doped TiO_2 nanocomposites (zeolite Y-c-TiO_2 nanocomposites) as new visible light–sensitive photocatalyst through hydrothermal treatment of zeolite mixed with Ti (IV) isopropoxide and sucrose as titanium precursor and carbon source, respectively, in contrast to the conventional hydrothermal method employing tetra butyl titanate as titanium precursor and glucose as carbon source (He et al. 2013), and investigated their physicochemical properties and solar photocatalytic activities on degradation of antibiotic, cefazolin, in water. Hence, the photocatalytic reaction of the as-prepared zeolite Y-c-TiO_2 nanocomposite was preliminarily evaluated by observing the photocatalytic degradation of methylene blue as a model reaction, exhibiting complete (100%) mineralization of methylene blue under the short-time irradiation of solar light. Accordingly, the nanocomposites exhibited highly efficient photocatalytic degradation of cefazolin. The present study also focused on the degradation pathway of cefazolin *via* LC-MS analysis, and the obtained results suggested the destruction of beta lactam ring in cefazolin which leads to the loss of antibiotic activity. To the best of our knowledge, no systematic assessment and degradation pathway are available on the photocatalytic degradation of cefazolin using carbon-doped TiO_2 supported by zeolite Y. Hence, this research aims to eliminate cefazolin toxicity from aqueous streams with the

aid of zeolite Y-*c*-TiO$_2$ photocatalyst. The results suggest that the new photocatalyst can be applied to efficient purification of medicinal wastewater under sunlight irradiation.

Experimental

Materials and methods

Analytical grade titanium (IV) isopropoxide [Ti(OC$_3$H$_7$)$_4$], zeolite Y, sucrose [C$_{12}$H$_{22}$O$_{11}$], and methylene blue dye [C$_{16}$H$_{18}$N$_3$SCl] were purchased from Sigma-Aldrich. The antibiotic, cefazolin [C$_{14}$H$_{14}$N$_8$O$_4$S$_3$], was obtained from Sance Laboratories Pvt. Ltd., Kerala. All chemicals were used without additional purification methods. Distilled water was used all over the experiments.

Synthesis of zeolite Y-supported carbon-doped TiO$_2$ nanocomposites

The photocatalyst, zeolite Y-*c*-TiO$_2$ nanocomposite, was prepared via hydrothermal reaction. For this, 0.5 g of zeolite Y was mixed with 5.0 mL Ti(IV) isopropoxide, followed by the addition of 0.03 g of sucrose dissolved in 10.0 mL of water. The mixture was stirred well, and distilled water was further added till the white precipitate formation was stopped. The pH of the sol was then adjusted to 7.0 and was then subjected to hydrothermal reaction at 180 °C for 2 h. The same experimental process was adopted to get zeolite Y-supported TiO$_2$ (zeolite Y-TiO$_2$), excluding the step involving the addition of sucrose. Undoped TiO$_2$ was also synthesized by the same procedure without the addition of sucrose and zeolite Y.

Characterizations

Fourier transform infrared (FT-IR) spectral analysis of the synthesized samples were examined in a Perkin Elmer spectrum Two FT-IR Spectrometer in the range 4000-400 cm^{-1}. X-ray diffraction patterns (XRD) were recorded on a Rigaku Miniflex 600 diffractometer using Cu Kα (λ = 0.15418 nm) radiation in the range of 5–80°. Scanning electron microscopy combined with energy-dispersive X-ray analysis (SEM-EDX) of the samples was analyzed using a Jeol 6390LA/OXFORD XMX N instrument. Transmission electron microscopic images (TEM) of the samples were recorded on a Jeol/JEM-2100 field emission electron microscope. The X-ray photoelectron spectroscopy (XPS) analysis was executed on a Kratos Axis Ultra X-ray photoelectron spectrometer, with Al Kα radiation as the exciting source. The specific surface area of the samples was measured using Brunauer-Emmett-Teller (BET) surface area analyzer (Tristar II, Micrometrics, USA). The diffuse reflectance spectra (DRS) of the samples were executed using a
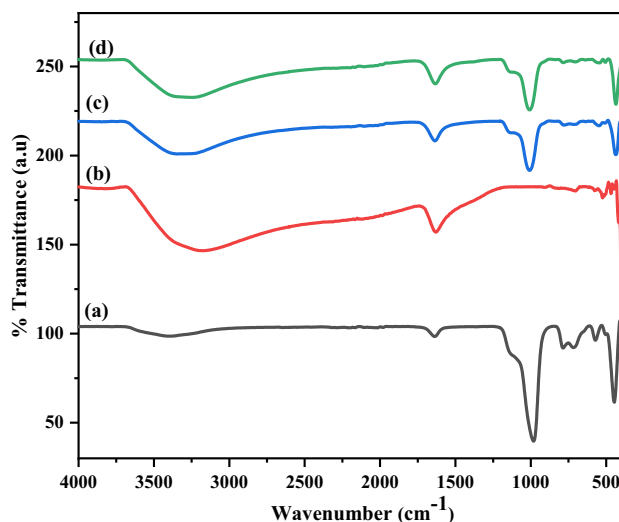
Fig. 1 FT-IR spectra of (a) zeolite Y, (b) TiO$_2$, (c) zeolite Y-TiO$_2$, and (d) zeolite Y-*c*-TiO$_2$

UV-2600 Shimadzu UV-visible spectrophotometer. The photoluminescence (PL) spectral measurements were performed using the Fluorolog Horiba spectrofluorometer. Systronics 2203 Double beam UV-Vis spectrophotometer was used to evaluate the photocatalytic activity of the synthesized nanocomposites. The intermediate products formed during the degradation process, and the mechanistic pathways were investigated by a liquid chromatography-mass spectrometer (LC-MS, Shimadzu, Japan).

Photocatalytic activity measurements

The photocatalytic degradation of methylene blue dye solution was assessed using the synthesized bare TiO$_2$, zeolite Y-TiO$_2$, and zeolite Y-*c*-TiO$_2$ samples. For a typical photocatalytic experiment, 500 mg L^{-1} of synthesized samples was suspended separately in 30 mL of 50 mg L^{-1} methylene blue (MB) aqueous solution. The suspension thus obtained was equilibrated by stirring in the dark for 30 min. After equilibration, the sample solution was irradiated with solar simulator (Heber Scientific, model no: HMV-88123) which consists of visible light source (tungsten halogen lamp) and UV light source (mercury vapor lamp) with A.M 1.5G filter. The samples were collected at different time intervals, and they were centrifuged to measure the absorbance of methylene blue solution at 660 nm using a Systronics 2203 Double beam spectrophotometer. The % degradation of dye solution was evaluated using the equation $\frac{C_0 - C_t}{C_0} \times 100$, where C_0 and C_t denote the initial and final concentration of MB dye solution. When using solar light irradiation alone or in the absence of the photocatalyst, there was no degradation observed for MB.
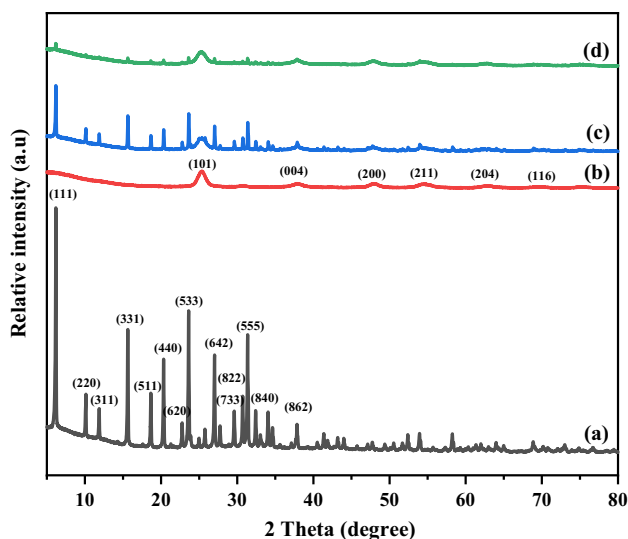
Fig. 2 XRD patterns of the synthesized samples: (a) zeolite Y, (b) TiO$_2$, (c) zeolite Y-TiO$_2$, and (d) zeolite Y-*c*-TiO$_2$

The degradation of the cephalosporin antibiotic, cefazolin, was investigated using the most active catalyst, zeolite Y-supported carbon-doped TiO$_2$ (zeolite Y-*c*-TiO$_2$). For this study, 500 mg L^{-1} of zeolite Y-*c*-TiO$_2$ was added into 30 mL cefazolin solution with a concentration of 50 mg L^{-1}. Prior to solar light irradiation, the solution containing cefazolin and catalyst was stirred in the dark for 30 min to attain adsorption-desorption equilibrium. At regular time intermissions, 5.0 mL aliquots were separated from the suspension and directly centrifuged and examined by recording disparities of the absorbance at the absorption band maximum (273 nm) of cefazolin using a Systronics 2203 Double beam spectrophotometer. The degradation intermediates formed during the photocatalytic removal of cefazolin were investigated by taking liquid chromatography-mass spectroscopy (LC-MS) of the aliquots of cefazolin after 0 min, 180 min, and 360 min of solar irradiation. Electrospray ionization in positive ion mode (ES+) was executed to get the mass spectra, and the mobile phase used was 0.1% formic acid in water (15%) and acetonitrile (85%) in isocratic mode. The degradation pathway of cefazolin was proposed using the mass spectra analysis, which provided evidence concerning various intermediates.

Analysis of photocatalytic mechanism

To study the involvement of active radical species in the degradation process of MB, isopropyl alcohol (IPA), ascorbic acid (AA), and ammonium oxalate (AO) were used to capture $^{\bullet}$OH, $^{\bullet}$O$_2^-$, and h$^+$, respectively. The experimental backgrounds were like the photocatalytic activity test for MB degradation.

The hydroxyl radicals ($^{\bullet}$OH) formed during the photocatalytic reaction process can be detected from the reaction between coumarin and photocatalysts. For this experiment, 20.0 mL of coumarin aqueous solution (10^{-4} M) was added to 500 mg L^{-1} of photocatalyst and placed under sunlight after permitting it to reach the adsorption-desorption equilibrium in the dark. The photoluminescent intensity of the reaction solution at various time intervals was then measured at an excitation wavelength of 332 nm.

The formation of superoxide radicals was detected by studying the absorption of nitro blue tetrazolium (NBT) aqueous solution treated with photocatalyst. For this study, 5×10^{-5} M NBT solution (20.0 mL) was mixed with 500 mg L^{-1} of photocatalyst and kept under solar light irradiation after 30 min of stirring in dark. The generation of $^{\bullet}$O$_2^-$ radicals was then examined by observing the absorption of NBT solution using UV-Vis spectrophotometer at 259 nm.
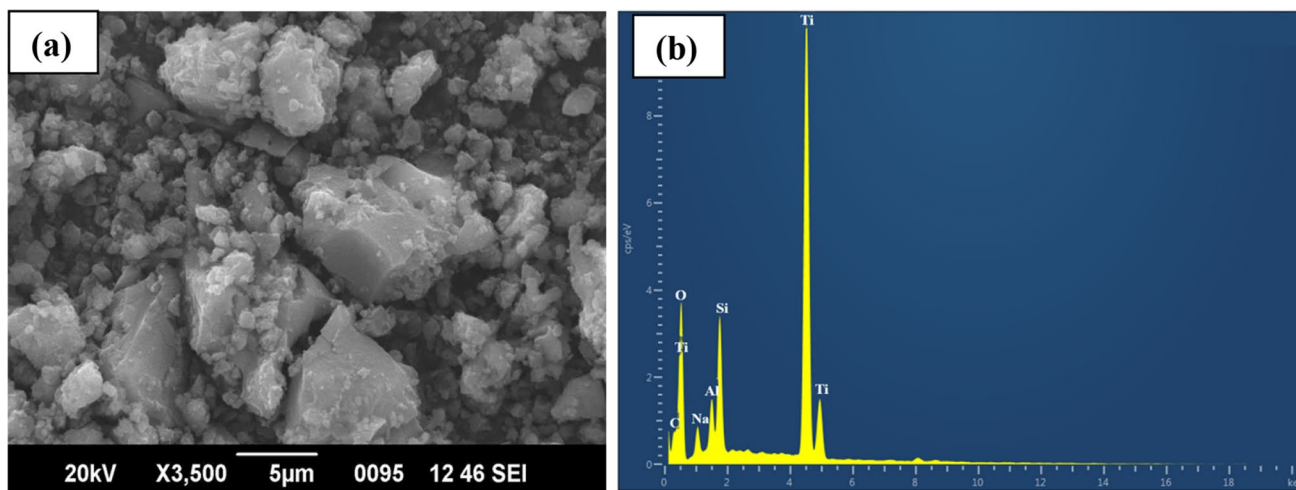
Fig. 3 **a** SEM image and **b** EDX spectrum of zeolite Y-*c*-TiO$_2$

Fig. 4 **a** TEM image, **b** HR-TEM image, and **c** SAED pattern of zeolite Y-*c*-TiO$_2$
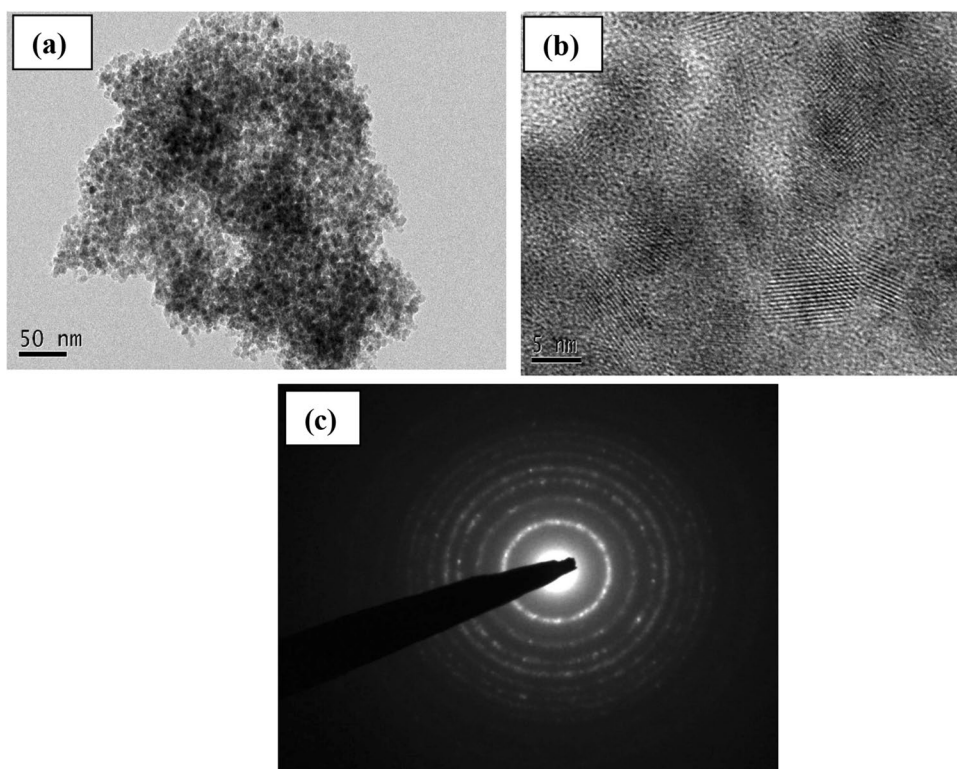
Results and discussion

Surface morphology and structural characterization

In order to investigate the interaction between TiO$_2$ and zeolite Y in the synthesized zeolite Y-*c*-TiO$_2$ nanocomposite, FT-IR spectra of zeolite Y-*c*-TiO$_2$ and zeolite Y-TiO$_2$ nanocomposites were measured and compared with that of zeolite Y or TiO$_2$ nanoparticles as shown in Fig. 1. The prominent IR peaks of zeolite Y (Fig. 1(a)) and TiO$_2$ (Fig. 1(b)) nanoparticles were retained in both spectra of zeolite Y-TiO$_2$ (Fig. 1(c)) and zeolite Y-*c*-TiO$_2$ (Fig. 1(d)) catalysts, supporting the existence of TiO$_2$ nanoparticles and zeolite Y in zeolite Y-TiO$_2$ and zeolite Y-*c*-TiO$_2$ nanocomposite samples. In the spectra of zeolite Y-TiO$_2$ and zeolite Y-*c*-TiO$_2$, there noticed a slight shift in the bands/peaks position and also a change in the band intensity which may be credited to the existence of carbon as a dopant. No new bands were noticed after doping carbon into zeolite Y-TiO$_2$. All the samples exhibited a strong broad peak in the range of 3000–3400 cm^{-1} and a small peak in the range of 1620–1640 cm^{-1} which can be attributed to the stretching and bending vibrations of the H-O-H group, respectively (Wang et al. 2012).

The weak peaks which appeared around 524 cm^{-1} and 466 cm^{-1} in the IR spectrum of TiO$_2$ are due to the vibration of the Ti-O bond (Mahalingam et al. 2017). The Si-O, SiO-Al, and Al-OH asymmetric and symmetric stretching vibrations agreeing to the internal TO$_4$ (T = Si, Al) structure

of zeolite Y at 984 cm^{-1} display an obvious red shift in the cases of zeolite Y-TiO$_2$ and zeolite Y-*c*-TiO$_2$, which appear at 1008 cm^{-1} and 1010 cm^{-1}, respectively (Mekki et al. 2020). This outcome established the effect of the Ti species on the framework of zeolite. The bands at 1140 and 788 cm^{-1} signify the asymmetric and symmetric stretching vibrations in the external TO$_4$ structure (T = Si, Al) of zeolite Y (Mekki et al. 2020). The band appeared at 572 cm^{-1} related to the double ring external linkage of zeolite Y is blue shifted by 24 cm^{-1} and 30 cm^{-1} in case of zeolite Y-TiO$_2$ and zeolite Y-*c*-TiO$_2$ composites, respectively (Mekki et al. 2020). The absence of antisymmetric stretching vibration of the Ti-O-Si bond in the range 950–960 cm^{-1} implies that TiO$_2$ is probably encapsulated within the zeolite voids without any strong chemical interaction between them (Zhang et al. 2010). The wide-ranging peak presented between 800 and 400 cm^{-1} in zeolite Y-TiO$_2$ and zeolite Y-*c*-TiO$_2$ samples may be due to the superposition of Ti-O and Si-O bonds (Wang et al. 2012).

Figure 2 shows XRD patterns of the synthesized samples. The diffraction pattern of TiO$_2$ nanoparticles (Fig. 2(b)) confirms the presence of anatase (JCPDS-21-1272) phase (Nagaraj et al. 2020). The diffraction pattern of the zeolite Y (Fig. 2(a)) exhibits that it is highly crystalline, revealing the reflections typical to zeolite Y as reported in literature (Mekki et al. 2020; Treacy and Higgins 2001). The XRD patterns of the composite samples zeolite Y-TiO$_2$ (Fig. 2(c)) and zeolite Y-*c*-TiO$_2$ (Fig. 2(d)) displayed crystallinity

Fig. 5 XPS spectra of **a** survey scan, **b** Ti2p, **c** O1s, **d** C1s, **e** Si2p, and **f** Al2p of zeolite Y-c-TiO$_2$ nanocomposite
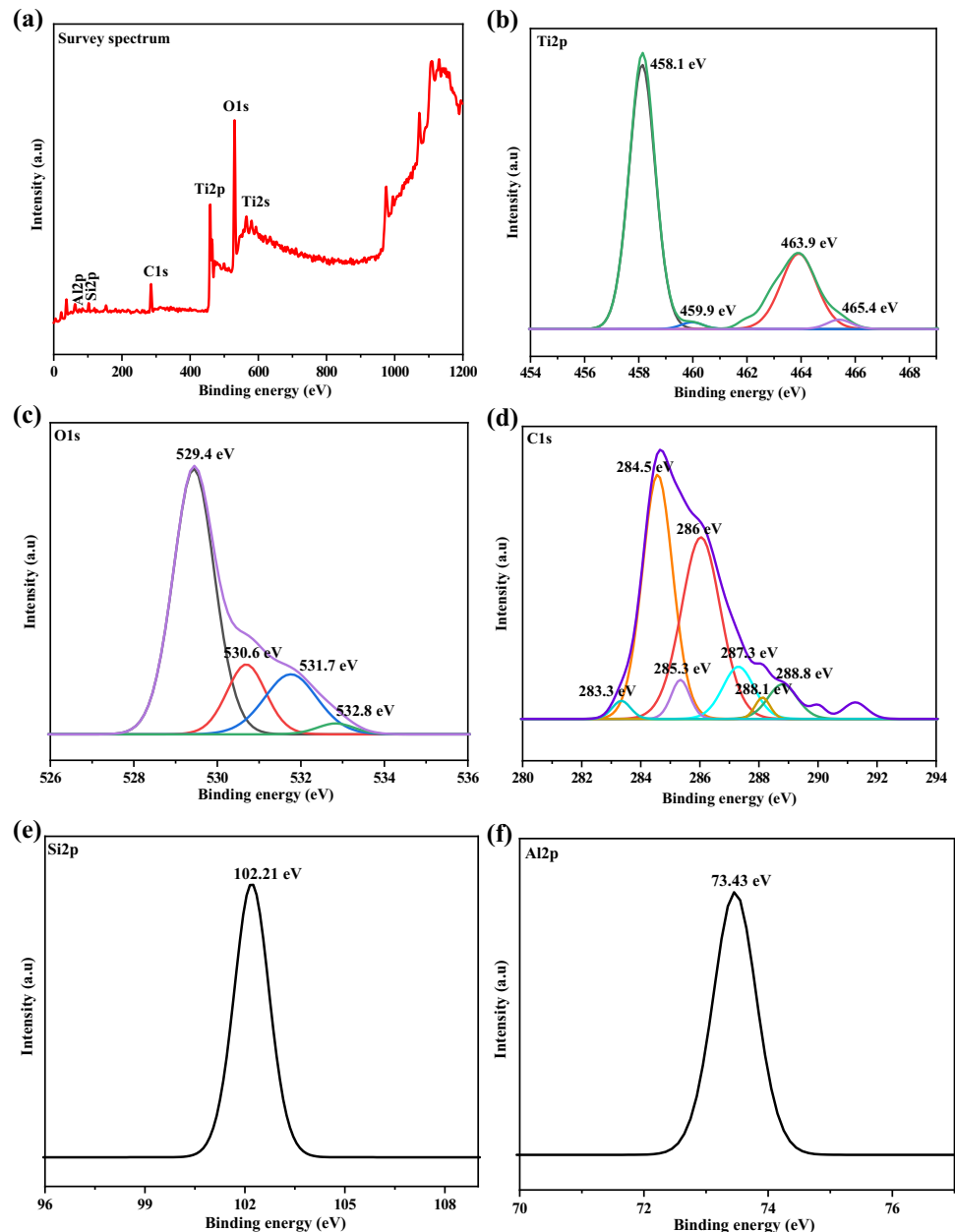
analogous to that of zeolite Y along with anatase phase TiO$_2$. The peak locations of the zeolite in the diffractogram pattern of zeolite Y-TiO$_2$ are not altered by the integration of TiO$_2$, supporting that TiO$_2$ is in captured form in the cages or cavities of zeolite, and it thereby authorizes that zeolite framework has not varied with the incorporation of TiO$_2$. The encapsulated TiO$_2$ gradually occupies the cavities of the zeolite, which leads to a declination in the intensity of XRD peaks (Easwaramoorthi and Natarajan 2009).

The crystallite size of the synthesized TiO$_2$ nanoparticles was assessed using Scherrer's equation; $D_{XRD} = 0.9\lambda/\beta \cos\theta$, where D is the crystallite size, λ is the wavelength of X-ray used, and β and θ are full width at half maximum intensity

(FWHM) of XRD diffraction lines and half diffraction angle 2θ, respectively (Zhang et al. 2019). The average crystallite size of TiO$_2$ is evaluated to be 6 nm.

The morphology and elemental composition of the zeolite Y-c-TiO$_2$ nanocomposites were further characterized by SEM-EDX and TEM analysis. Figure 3(a) shows the SEM image of the prepared nanocomposite, exhibiting mostly cubic crystals of zeolite Y, even though it is difficult to specify incorporation with c-TiO$_2$. Nevertheless, the crystal surface looks non-porous in contrast to the typical porous surface of pure zeolite-Y as reported (Jansson et al. 2015). This again supports encapsulation of c-TiO$_2$ nanoparticles in the zeolite cavities through the coprecipitation after
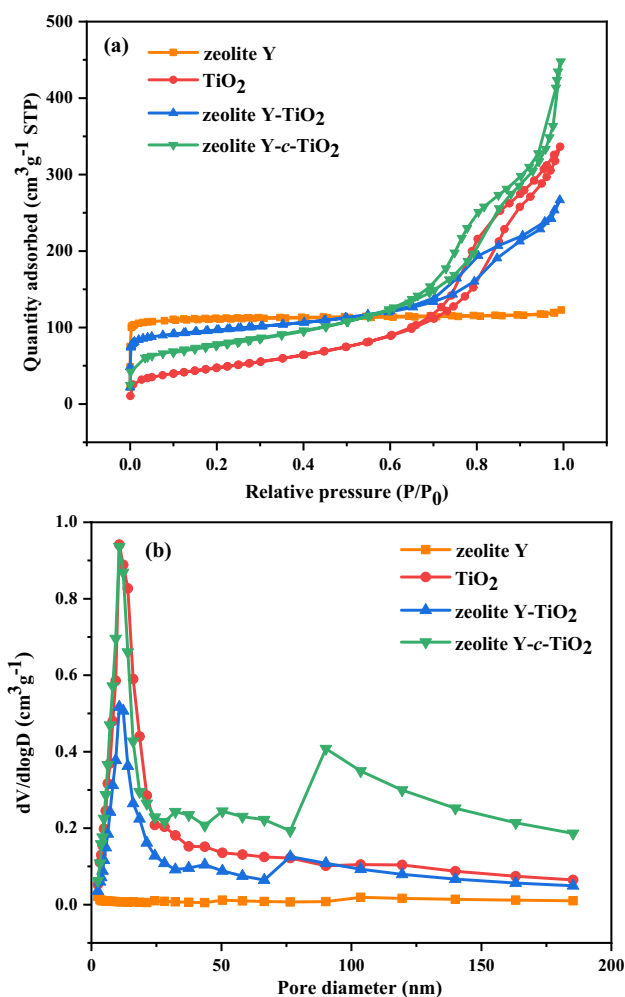
Fig. 6 **a** N$_2$ adsorption-desorption isotherms and **b** Barrett-Joyner-Halenda (BJH) adsorption pore size distribution of the synthesized photocatalysts

Table 1 BET surface area, pore volume, and pore diameter distribution of prepared samples

Samples	Surface area (m^2 g^{-1})	Pore volume (cm^3 g^{-1})	Pore diameter (nm)
Zeolite Y	449.5	0.1882	1.675
TiO$_2$	173.12	0.5144	11.884
Zeolite Y-TiO$_2$	360.75	0.4093	4.538
Zeolite Y-c-TiO$_2$	274.73	0.6645	9.675

hydrothermal reaction of all the components. The efficacious incorporation of c-TiO$_2$ nanoparticles in the zeolite matrix could be confirmed from detection of C and Ti together with Al, Si, and Na elements on the EDX spectrum (Fig. 3b).

Figure 4a and b show low- and high-resolution TEM images of zeolite Y-c-TiO$_2$ nanocomposite, respectively. The low-resolution TEM image displays some dark colored

region, suggesting that the zeolites have a certain thickness with dispersion of c-TiO$_2$ nanoparticles in zeolite Y as supported by the high-resolution TEM image which exhibits the dark shadow over the zeolite crystalline lattice. The good dispersion of TiO$_2$ nanoparticles in zeolite Y may also be due to cracking of their aggregation inside the microporous cages (Aprile et al. 2008), endorsing their exposure in photodegradation process. Even though XPS spots carbon species in zeolite Y-c-TiO$_2$ nanocomposite, its existence is not discovered by transmission microscope imaging because of the lower surface concentration of carbon species. The particle sizes were found to be less than 10 nm which agrees with the crystallite size obtained from XRD patterns. The selected area electron diffraction (SAED) pattern (Fig. 4c) exhibited that zeolite Y-c-TiO$_2$ nanocomposite possesses a uniform polycrystalline structure.

The surface chemical bonding in the zeolite Y-c-TiO$_2$ system was further studied using X-ray photoelectron spectroscopy (XPS) analysis (Fig. 5). The survey spectrum depicted in Fig. 5a shows the presence of Ti, O, C, Si, and Al peaks in the XPS spectrum. Specifically, in the Ti2p spectrum (Fig. 5b), two peaks observed at 458.1 eV and 463.9 eV are associated with the Ti2p$_{3/2}$ and Ti2p$_{1/2}$ of TiO$_2$, respectively (Oseghe and Ofomaja 2018). As per the reports of Akhavan and Ghaderi, the weak peaks existing at 459.7 eV and 465.4 eV (relating to Ti2p$_{3/2}$ and Ti2p$_{1/2}$ peaks) could be ascribed to Ti-C bond which supports again the doping of carbon into TiO$_2$ (Akhavan and Ghaderi 2009).

The O1s spectrum (Fig. 5c) of zeolite Y-c-TiO$_2$ comprises four peaks positioned at 529.4, 530.6, 531.7, and 532.8 eV. The peaks at 529.4 eV and 532.8 eV correspond to Ti-O and C-O-Tii bonds, respectively (Bao et al. 2021). The binding energy peaks appeared at 531.7 eV and 530.6 eV were related to the surface adsorbed oxygen and hydroxyl groups (Bao et al. 2021; Li et al. 2020).

In the C1s spectra of zeolite Y-c-TiO$_2$ (Fig. 5d), seven main peaks were detected, which correspond to (i) O-Ti-C bond formed due to the substitution of oxygen in the TiO$_2$ lattice by carbon (283.3 eV) (He et al. 2013; Negi et al. 2021), (ii) adventitious elemental carbon impurities as well as the organic residues of the sample (284.5 eV) (He et al. 2013; Huang et al. 2021; Ren et al. 2007), (iii) C-OH (285.3 eV) (Jing et al. 2020), (iv) C-O (286 eV) (Huang et al. 2021), (v) C-O-C (287.3 eV) (Jing et al. 2020; Xing et al. 2014), (vi) C=O (288.1 eV) (Park et al. 2015), and (vii) Ti-O-C structure formed due to the substitution of some lattice titanium atoms by carbon (288.8 eV) (Shao et al. 2017; Bao et al. 2021).

The peaks located at binding energies 102.21 eV and 73.43 eV were attributed to Si2p (Fig. 5e) and Al2p states (Fig. 5f) in zeolite Y, respectively (Kadi et al. 2019).

The specific surface areas and porosity in the structure of the zeolite Y, TiO$_2$, zeolite Y-TiO$_2$, and zeolite Y-c-TiO$_2$
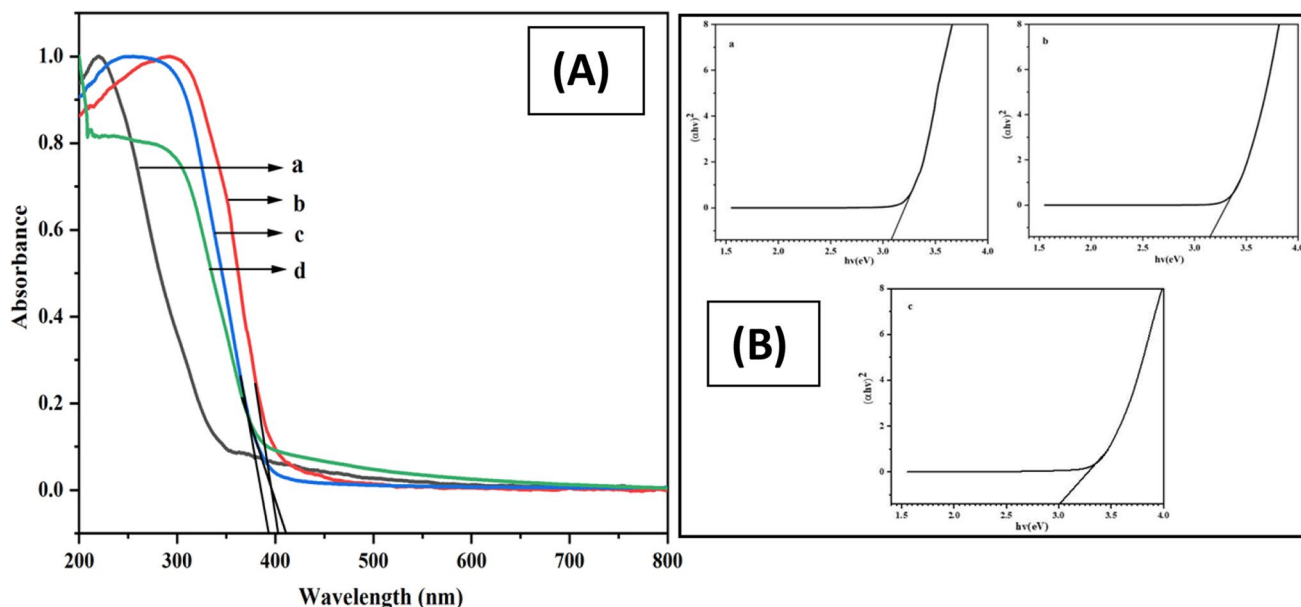
Fig. 7 **A** The UV-Vis diffuse reflectance spectra of (a) zeolite Y, (b) TiO$_2$, (c) zeolite Y-TiO$_2$, and (d) zeolite Y-c-TiO$_2$ and **B** Plot of $(\alpha h\nu)^2$ against photon energy ($h\nu$) of (a) TiO$_2$, (b) zeolite Y-TiO$_2$, and (c) zeolite Y-c-TiO$_2$

Table 2 Band gap of the synthesized samples

Samples	Absorption edge (nm)	Band gap (eV) obtained from $E_g = 1239.8/\lambda$	Band gap value (eV) obtained from $(\alpha h\nu)^2$ to $h\nu$ plot
TiO$_2$	402	3.08	3.08
Zeolite Y-TiO$_2$	393	3.15	3.15
Zeolite Y-c-TiO$_2$	412	3.00	3.00
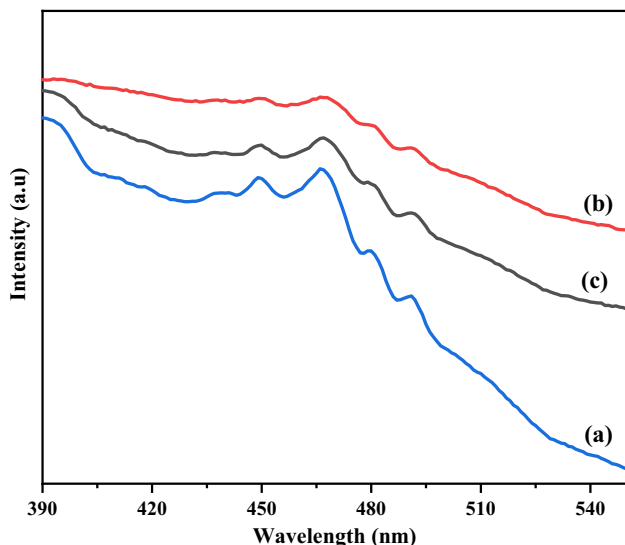
Fig. 8 Photoluminescence spectrum of (a) TiO$_2$, (b) zeolite Y-TiO$_2$, and (c) zeolite Y-c-TiO$_2$ (excitation wavelength = 380 nm)

samples were examined by their nitrogen adsorption-desorption isotherms (Fig. 6a) and BJH pore size distribution plots (Fig. 6b).

As described in IUPAC classification, the zeolite Y is matching to the type I isotherm, which is representative of the microporous solids and others displayed a capillary condensation loop at a relative pressure, higher than 0.4, which specified that the samples (TiO$_2$, zeolite Y-TiO$_2$, and zeolite Y-c-TiO$_2$) owned substantial features of mesoporous materials (Abbas et al. 2020; Diao et al. 2019). The type IV isotherm displayed by TiO$_2$ nanoparticles is associated with the textural porosity existing between TiO$_2$ particles (Guesh et al. 2016). After the loading of TiO$_2$ on zeolite, zeolite Y-TiO$_2$ was bestowed with a reduction of the BET specific surface area attributable to the dispersion of TiO$_2$ nanoparticles in the micropores of zeolite Y, thereby making the micropores of zeolite Y jammed (Guesh et al. 2016; Zhang et al. 2018). The N$_2$ adsorption-desorption isotherms of the zeolite Y-c-TiO$_2$ powders are also type IV as per IUPAC,

which shows its mesoporous nature. The hysteresis loop noticed in zeolite Y-*c*-TiO$_2$ in the range of 0.55 < P/Po < 0.99 is resulting from slit-like pores (Abbas et al. 2020). The significant reduction in the surface area of zeolite Y-TiO$_2$ after carbon doping is good evidence of successful incorporation of carbon source.

From the BJH plot, clearly the pore volume of zeolite Y-TiO$_2$ upsurges compared to zeolite Y, owing to the mesoporous structure provided by TiO$_2$ nanoparticles. Furthermore, a significant increase in pore volume and pore diameter upon carbon doping makes zeolite Y-*c*-TiO$_2$, a more efficient photocatalyst by enhancing the adsorption of toxic contaminants which agrees with previous reports (Zhang et al. 2018; Amran et al. 2019). Table 1 shows the BET surface area, pore volume, and pore diameter distribution of prepared samples. The porous zeolite Y possessing large surface area is a good support for the dispersion of carbon-doped TiO$_2$ nanoparticles. The aggregation of particles is verboten after the integration of zeolite Y to carbon-doped TiO$_2$. The zeolite Y-supported carbon-doped TiO$_2$ sample will positively offer more surface area to absorb arriving photons as well as to adsorb contaminant molecules (Li et al. 2020).
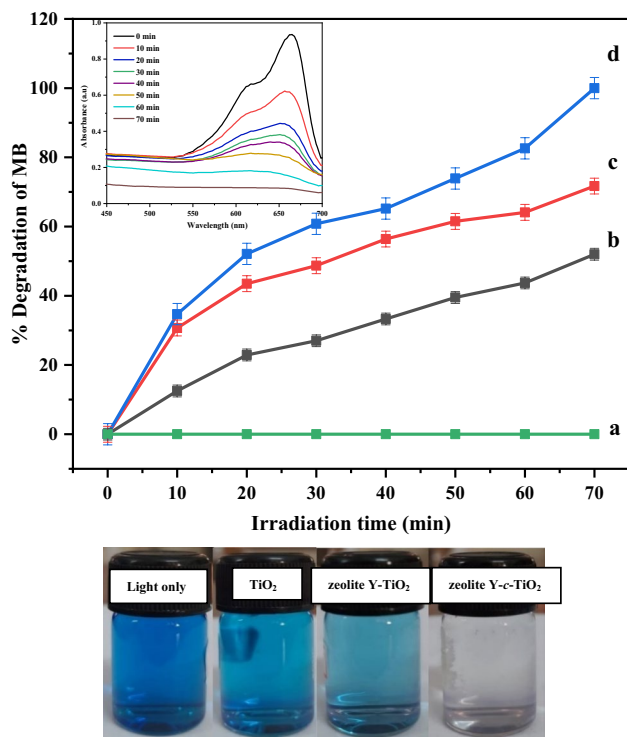
Optical properties

In order to investigate optical properties, UV-Vis diffuse reflectance and photoluminescence spectral studies were carried out. Figure 7A shows the UV-Vis diffuse reflectance spectra (UV-Vis DRS) analysis for TiO$_2$, zeolite Y-TiO$_2$, and zeolite Y-*c*-TiO$_2$. UV region of both zeolite Y-TiO$_2$ and zeolite Y-*c*-TiO$_2$ shows a considerable blue shift with respect to free TiO$_2$ nanoparticles due to the quantum confinement effect of the TiO$_2$ nanoparticles lodging inside the voids of zeolite Y (Alvaro et al. 2006). However, zeolite Y-*c*-TiO$_2$ exhibited much higher absorption of visible light beyond 400 nm as compared to both free TiO$_2$ and zeolite Y-TiO$_2$. The equation $E_g = 1239.8/\lambda$ was used to measure the band gap energies of the samples. In this equation, E_g is the band gap (eV) and λ (nm) is the wavelength of the absorption edges in the spectrum (O'regan and Grätzel 1991, Chuang et al. 2015).

Tauc plot ($h\upsilon$-$(\alpha h\upsilon)^2$) was also plotted (Fig. 7B) to estimate the band gap energy of synthesized nanosemiconductors, where α is the absorption coefficient, h is the Planck constant, and υ is the light frequency. The $h\upsilon$-$(\alpha h\upsilon)^2$ plot is valid to direct-band gap material. The results obtained are given in Table 2, and it demonstrates that carbon doping and the zeolite loading decreased the band gap and increased the visible light absorption of TiO$_2$.

The photoluminescence emission spectra (PL) of TiO$_2$, zeolite Y-TiO$_2$ and zeolite Y-*c*-TiO$_2$ samples were studied in the range of 390–550 nm to examine the separation efficiency of photo-induced charge carriers, and the results are depicted in Fig. 8. It is evident that all the samples exhibit PL signal centered around 467 nm, which is an outcome of surface oxygen vacancies and defects in TiO$_2$ (Wang et al. 2012). The PL intensities of the samples decrease in the

Fig. 9 Degradation and corresponding photographs of MB in presence of (a) light only, (b) TiO$_2$, (c) zeolite Y-TiO$_2$ and (d) zeolite Y-*c*-TiO$_2$ under 70 min of solar light irradiation (the error bars correspond to standard deviation). (Inset shows the UV-Vis absorption spectra of the time dependent photodegradation of MB in the presence of zeolite Y-*c*-TiO$_2$)
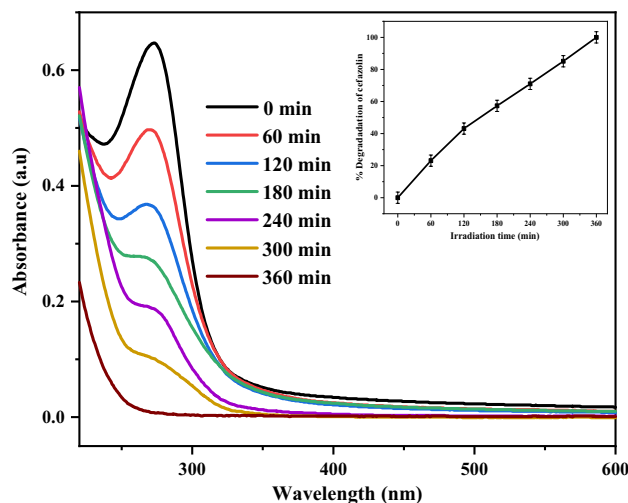
Fig. 10 UV-Vis absorption spectra of the time dependent photodegradation of cefazolin in the presence of zeolite Y-*c*-TiO$_2$ (Inset shows the photocatalytic degradation of cefazolin in the presence of zeolite Y-*c*-TiO$_2$. (The error bars correspond to standard deviation))
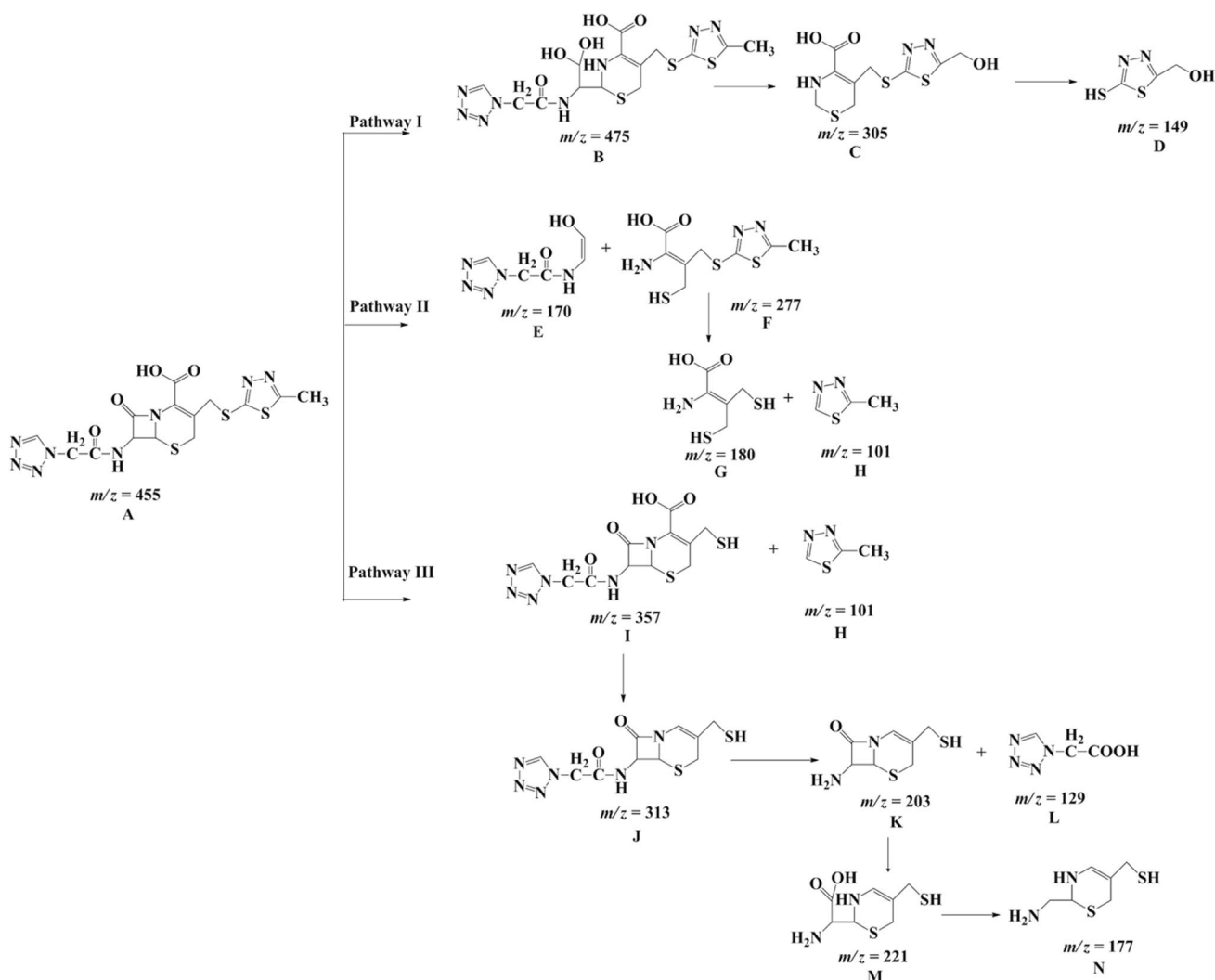
Scheme 1 Degradation pathway of cefazolin

order zeolite Y-TiO$_2$ > zeolite Y-c-TiO$_2$ > TiO$_2$. The zeolite-incorporated TiO$_2$ samples exhibit much higher PL intensity than bare TiO$_2$ as zeolite upsurges the oxygen vacancy and intrinsic defects of TiO$_2$. The enhancement in oxygen vacancies and defects makes PL signals stronger which contributes to higher photocatalytic activity (Xiao et al. 2007). Generally, a lower PL intensity specifies a lower recombination rate of excitons (electron-hole pairs) as well as higher separation efficiency which leads to improved photocatalytic activity (Wang and Li 2014). The PL intensity of zeolite Y-c-TiO$_2$ nanocomposite is lesser than that of zeolite Y-TiO$_2$, demonstrating the role of carbon doping in the separation of electron-hole pairs.

Photocatalytic activity

The solar light photocatalytic activities of the synthesized photocatalysts were assessed by observing degradation of methylene blue as a model pollutant in water, and the results are portrayed in Fig. 9. The photocatalytic activity increases in the order TiO$_2$ < zeolite Y-TiO$_2$ < zeolite Y-c-TiO$_2$, indicating that the use of the zeolite Y, as a support in the zeolite Y-TiO$_2$ system, plays a crucial role in enhancing the photocatalytic degradation of pollutants. In the adsorption process before solar light irradiation, the methylene blue adsorbed by anatase TiO$_2$ was quite low and was greatly enhanced by zeolite incorporation. The incorporation of zeolite onto TiO$_2$ expands the photodegradation ability of TiO$_2$ by providing high surface area, good adsorption property, and ability to disperse TiO$_2$ nanoparticles. The result also specifies that the photocatalytic activity of zeolite Y-TiO$_2$ can be significantly enhanced with carbon doping. Almost 100% of methylene blue was mineralized to exhibit bleached water by the zeolite Y-c-TiO$_2$ system within 70 min as displayed in the picture of the dye
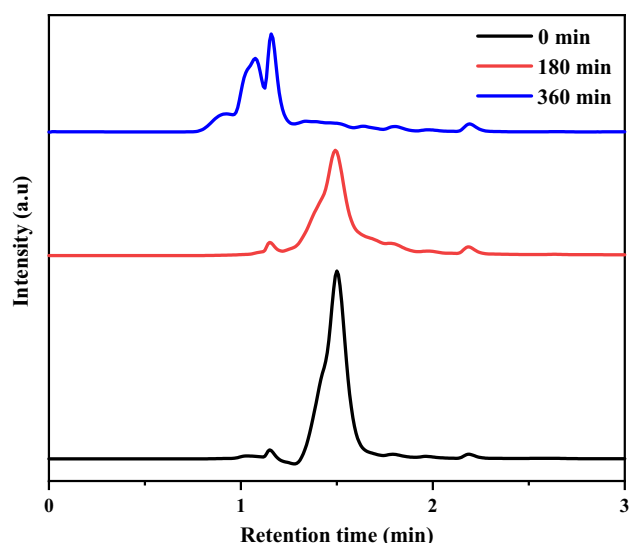
Fig. 11 HPLC (254 nm) chromatograms of cefazolin solution in the presence of zeolite Y-*c*-TiO$_2$ during different degradation times under sunlight

solution bottles in Fig. 9. The high visible light absorption and prolonged separation between the photoinduced charge carriers (excitons) assisted the improvement of photocatalytic activity of the zeolite Y-*c*-TiO$_2$ sample. Since C-doped TiO$_2$ is a good visible light responsive photocatalyst and zeolite Y is a good adsorbent, the coupling of these two effects could result in a synergistic outcome on photocatalysis.

Subsequently, for the purpose to develop the solar photocatalysts to purify medicinal wastewater, the solar photocatalytic activities of zeolite Y-*c*-TiO$_2$ was evaluated on the degradation of the antibiotic, cefazolin, dissolved in water, and the results are shown in Fig. 10.

The absorption maxima of cefazolin at 273 nm drops to zero within 360 min of solar light irradiation, and complete degradation of cefazolin would be anticipated in this time. To inspect the various intermediates formed during the degradation process and to predict the degradation pathway, samples were withdrawn at 0 min, 180 min, and 360 min of solar light irradiation and are named as S$_0$, S$_{180}$, and S$_{360}$, respectively. Mass spectra of the samples (S$_0$, S$_{180}$, and S$_{360}$) were obtained from LC-MS analysis, in which sample ionization was made through electrospray ionization in positive mode. The three possible degradation pathways for cefazolin degradation are shown in Scheme 1.

The positive ionization of cefazolin generated protonated molecular ions [M + H]$^+$. In sample (S$_0$), cefazolin with a molecular mass of 454 was spotted at *m/z* 455 (A). With an increase in the irradiation time, the ion peak of *m/z* 455 slowly diminished and some extra ion peaks are appearing,

which directed to the assumption that the antibiotic cefazolin have been degraded. In path 1, the hydrolysis product appeared at *m/z* 475(B) was resulted from the β-lactam ring cleavage of cefazolin compound and this was escorted by hydroxyl radical attack on the methyl in thiadiazole, forming the monohydroxylated derivative C with *m/z* 305 (Chen et al. 2021). The C-S bond cleaves to form product D with *m/z* 149, which is 5-(hydroxymethyl)-1,3,4-thiadiazole-2(3H)-thione. In path 2, the formation of products E (*m/z* 170) and F (*m/z* 277) can be ascribed to the rupture of β-lactam from the initial compound A (*m/z* 455); later, F was further decomposed to G (*m/z* 180) and H (*m/z* 101) after C-S bond breakage. In path 3, the products I (*m/z* 357) and H (*m/z* 101) instigate with the rupture of C-S bond on the parent cefazolin; furthermore, I undergoes decarboxylation leading to the formation of J with *m/z* 313 which was further accompanied amide bond cleavage to form K (*m/z* 203) and L (*m/z* 129). The fracture of the beta ring existing in K produces M (*m/z* 221), which can be degraded to N (*m/z* 177) by decarboxylation.

The assessment of the mass spectral analysis for the samples, S$_{180}$ and S$_{360}$, provided a clear idea about the degradation pathway of cefazolin in presence of zeolite Y-*c*-TiO$_2$ by solar photocatalysis. Since the fracture of β-lactam ring could result in destruction of bacterial antimicrobial resistance, most of the degradation products that reported through LC-MS analysis possess lower risk to the ecosystem (Chen et al. 2021).

The HPLC method (with UV detection at 254 nm) was also employed to assess the changes occurring in cefazolin during the photocatalytic degradation process, and the results are displayed in Fig. 11. It is clear from the figure that the peak detected for cefazolin at the instigation of degradation slowly declined with increase in irradiation time signifying that cefazolin would be degraded to other molecules. These outcomes demonstrated the crucial role played by zeolite Y-*c*-TiO$_2$ photocatalyst in the degradation of cefazolin with the aid of sunlight.

Mechanism of photocatalytic degradation of pollutants

For the purpose of recognizing the mechanism behind the photocatalytic degradation process, free radical scavenging experiments were executed to spot the radicals involved in the degradation of methylene blue. Isopropyl alcohol (IPA), ascorbic acid (AA), and ammonium oxalate (AO) were used to quench hydroxide radicals ($^•$OH), superoxide radicals ($^•$O$_2^-$), and hole (h$^+$), respectively (Wang et al. 2019). The results are portrayed in Fig. 12a, and it specified a substantial quenching effect on the degradation of MB with trapping agents. The degradation decreases noticeably after the
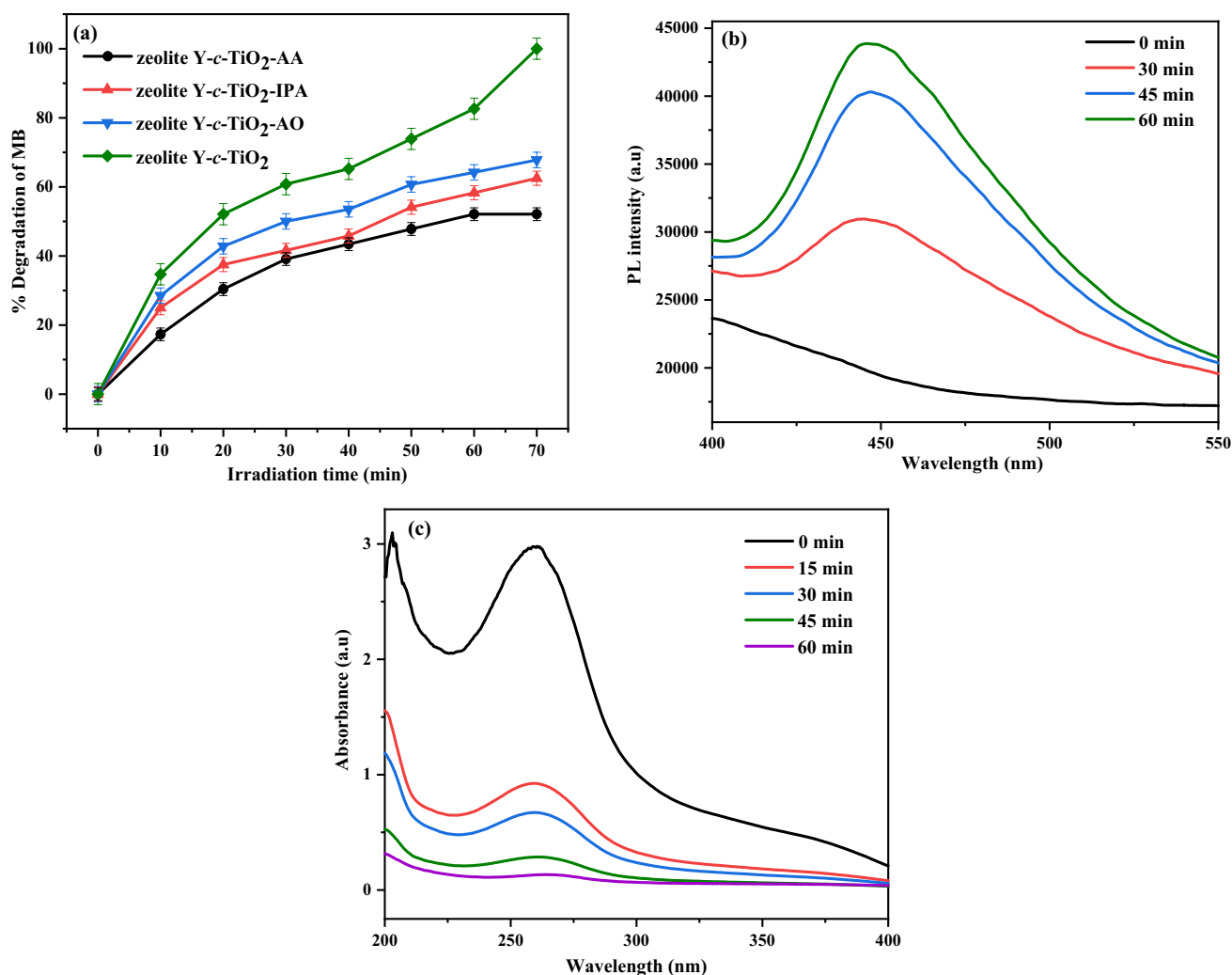
Fig. 12 **a** The percentage degradation of MB in the presence of zeolite Y-*c*-TiO$_2$ and different radical scavengers, **b** PL spectral changes observed during solar light irradiation of zeolite Y-*c*-TiO$_2$ dispersed in 10^{-4} M coumarin aqueous solution, and **c** UV-visible spectra of NBT in zeolite Y-*c*-TiO$_2$ dispersion under solar light irradiation

addition of AA, which validates $^{\bullet}O_2^-$ as the main active species in the photocatalytic degradation process of zeolite Y-*c*-TiO$_2$. The catalytic efficiency of the photocatalyst was only slightly reduced when the scavengers are IPA and AO, demonstrating that $^{\bullet}$OH and h$^+$ have least effect on the degradation of pollutants.

The generation of hydroxyl radicals in the photocatalytic system was confirmed by investigating the fluorescence spectral changes of coumarin solution treated with zeolite Y-*c*-TiO$_2$ photocatalyst under sunlight illumination (Fig. 12(b)) (Liang et al. 2016). A steady upsurge in PL emission intensity at about 450 nm is noticed with increase in irradiation time. This outcome can be credited to the reaction arising between coumarin and hydroxyl radicals formed on the zeolite Y-*c*-TiO$_2$ surface through photocatalytic reaction. In the absence of photocatalyst, no emission peak was observed for coumarin solution since

PL emission peak intensity is connected to the amount of $^{\bullet}$OH radicals formed during the photocatalytic reaction. Figure 12b thus confirms the generation of hydroxyl radicals during photocatalytic degradation reaction, which agrees well with the results of IPA quenching.

The production of $^{\bullet}O_2^-$ radicals was detected using the NBT method (Zhao et al. 2018). Figure 12c shows the UV-visible spectra of NBT solution mixed with zeolite Y-*c*-TiO$_2$ photocatalyst taken during different times of exposure to solar light. The absorption peak at 259 nm was found to be decreased with prolonged solar light irradiation due to the ability of NBT to trap $^{\bullet}O_2^-$ radicals evolved from the photocatalyst for the formation of formazan precipitate. The result supports the production of $^{\bullet}O_2^-$ radicals, which matches with the result of AA quenching.

The mechanism for the photocatalytic degradation of pollutants using the synthesized zeolite Y-*c*-TiO$_2$

Fig. 13 Mechanism of pollutant degradation using zeolite Y-*c*-TiO$_2$ under sunlight
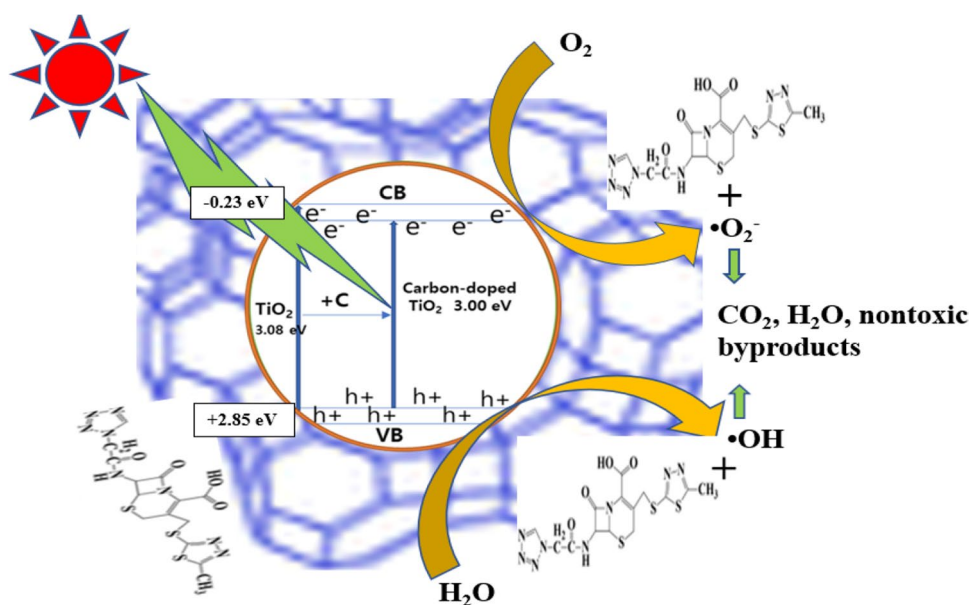
Fig. 14 a Cyclic runs of zeolite Y-*c*-TiO$_2$ for the degradation of cefazolin under solar irradiation (the error bars correspond to standard deviations) and **b** FT-IR spectra of zeolite Y-*c*-TiO$_2$ photocatalyst before and after five cyclic runs
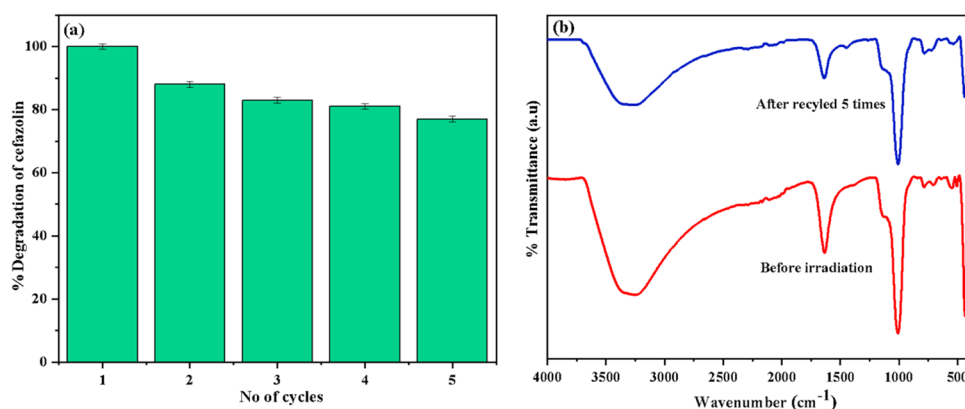
nanocomposite in relation with band gap values has been shown in Fig. 13. Tauc plot sketched using DRS spectra presented the band gap energy (E_g) of TiO$_2$ as 3.08 eV. The conduction band (E_{CB}) potential and valence band (E_{VB}) potential were calculated using the equations,

$$E_{VB} = \chi - E^e + 0.5\,E_g$$

$$E_{CB} = E_{VB} - E_g$$

χ is the electronegativity of TiO$_2$ (5.81 eV), and E^e (4.5 eV) is the energy of free electrons at hydrogen scale (Sharma et al. 2018). E_{VB} and E_{CB} were calculated to be 2.85 and −0.23 eV, respectively.

In *c*-TiO$_2$, the generation of electron (e$^-$) and holes (h$^+$) occurs by the excitation of valence band (VB) electrons to conduction band (CB) through the captivation of solar light. The photogenerated holes react with OH$^-$ or H$_2$O molecules adsorbed on the catalyst surface to produce hydroxyl radicals (•OH), whereas the excited electrons react with adsorbed O$_2$ to produce superoxide radicals (•O$_2^-$). The pollutant molecules can thus react with these reactive species to get mineralized into CO$_2$, H$_2$O, and other simple molecules. The carbon doping into the TiO$_2$ was useful in improving the photocatalytic activity because of its ability to prolong the separation between photoinduced charge carriers (e$^-$ and h$^+$). It adds new states in between the CB and VB of TiO$_2$, which results in band gap narrowing (Cinelli et al. 2017). Incorporation with zeolites facilitates transfer of the charge carriers (Yoon et al. 2007; Dutta and Severance 2011) to O$_2$ and water. In addition, it should be noted that the zeolites supporting *c*-TiO$_2$ serve as good adsorbents of the organic molecules, making close contact of the pollutants with the photogenerated oxidants for the enhanced photocatalytic activity (Noorjahan et al. 2004). Thus, the zeolite Y-*c*-TiO$_2$ can be used as a highly effective photocatalytic agent for the degradation of persistent organic medicines.

Recycling capacity of the catalyst

In the recoverability and reusability assessment of the synthesized zeolite Y-*c*-TiO$_2$ catalyst in the photocatalytic degradation of cefazolin under solar light irradiation, five repeated cycles were carried out, each lasting for 360 min. After each catalytic cycle, the used catalyst was separated by filtration and cleaned thoroughly with distilled water, dried, and then added to fresh cefazolin (50 mg L^{-1}) solution. From Fig. 14a, it is evident that the photocatalyst holds their catalytic activity after being recycled five times. Figure 14b depicts that the FT-IR spectrum of the recycled photocatalyst is identical to that of the pure photocatalyst. These outcomes point to the chemical stability and reusability of the synthesized photocatalyst. The decrease in the photocatalytic activity of zeolite Y-*c*-TiO$_2$ observed after five catalytic runs may be attributed to the loss of the catalyst during filtration and washing processes. The failure in thorough cleaning of the residual products adsorbed on the photocatalyst surfaces impacts the surface properties of the photocatalyst that also declines the catalytic activity (Huang et al. 2008).

Conclusion

In this study, zeolite Y-supported carbon-doped TiO$_2$ nanocomposites (zeolite Y-*c*-TiO$_2$) were successfully synthesized via hydrothermal route and were utilized for the degradation of cefazolin under solar light. The band gap energy of zeolite Y-*c*-TiO$_2$ was decreased (3.00 eV) when compared to that of undoped zeolite Y-TiO$_2$ nanocomposite (3.15 eV). Doping with carbon enhanced the visible light response under solar light irradiation, and the sample, zeolite Y-*c*-TiO$_2$, achieved near complete degradation for methylene blue and cefazolin within 70 min and 360 min, respectively. Radical scavenger experiment displayed that $\bullet O_2^-$ is the predominant active species in the aqueous suspension of zeolite Y-*c*-TiO$_2$ system, while contribution of $\bullet OH$ is secondary and photogenerated holes are the least. LC-MS analysis of cefazolin taken during different degradation stages demonstrated the cleavage of beta lactam ring, which could result in the destruction of antimicrobial resistance. Hence, zeolite Y-*c*-TiO$_2$ nanocomposite can be used as a potential candidate for the development of an environmentally sustainable photocatalytic treatment process for the purification of medicinal wastewater. The study offers a technically viable and inexpensive solution for environmental cleaning using sunlight in place of an artificial light.

Author contribution Conceptualization: Mekha Susan Rajan, Jesty Thomas; methodology: Mekha Susan Rajan, Jesty Thomas; formal analysis and investigation: Mekha Susan Rajan; writing — original draft preparation: Mekha Susan Rajan; writing — review and editing: Mekha Susan Rajan, Minjoong Yoon, Jesty Thomas; resources: Anju John; supervision: Jesty Thomas, Minjoong Yoon.

Data availability Not applicable.

Declarations

Ethics approval Not applicable.

Consent to participate Note applicable.

Consent for publication Not applicable.

Competing interests The authors declare no competing interests.

References

Abbas KK, Shabeeb KM, Aljanabi AAA, Al-Ghaban AMHA (2020) Photocatalytic degradation of Cefazolin over spherical nanoparticles of TiO$_2$/ZSM-5 mesoporous nanoheterojunction under simulated solar light. Environ Technol Innov 20:101070. https://doi.org/10.1016/j.eti.2020.101070

Akhavan O, Ghaderi E (2009) Photocatalytic reduction of graphene oxide nanosheets on TiO$_2$ thin film for photoinactivation of bacteria in solar light irradiation. J Phys Chem C 113:20214–20220. https://doi.org/10.1021/jp906325q

Ali T, Tripathi P, Azam A, Raza W, Ahmed AS, Ahmed A, Muneer M (2017) Photocatalytic performance of Fe-doped TiO$_2$ nanoparticles under visible-light irradiation. Mater Res Express 4:015022. https://doi.org/10.1088/2053-1591/aa576d

Alvaro M, Carbonell E, Fornés V, García H (2006) Enhanced photocatalytic activity of zeolite-encapsulated TiO$_2$ clusters by complexation with organic additives and N-doping. ChemPhysChem 7:200–205. https://doi.org/10.1002/cphc.200500264

Amran SNBS, Wongso V, Halim NSA, Husni MK, Sambudi NS, Wirzal MDH (2019) Immobilized carbon doped TiO$_2$ in polyamide fibers for the degradation of methylene blue. J Asian Ceramic Soc 7:321–330. https://doi.org/10.1080/21870764.2019.1636929

Aprile C, Corma A, Garcia H (2008) Enhancement of the photocatalytic activity of TiO$_2$ through spatial structuring and particle size control: from subnanometric to submillimetric length scale. Phys Chem Chem Phys 10:769–783. https://doi.org/10.1039/B712168G

Bao S, Liu H, Liang H, Li C, Bai J (2021) Electrospinned silk-ribbon-like carbon-doped TiO$_2$ ultrathin nanosheets for enhanced visible-light photocatalytic activity. Colloids Surf A Physicochem Eng Asp 616:126289. https://doi.org/10.1016/j.colsurfa.2021.126289

Chen Y, Tian H, Zhu W, Zhang X, Li R, Chen C, Huang Y (2021) L-Cysteine directing synthesis of BiOBr nanosheets for efficient cefazolin photodegradation: The pivotal role of thiol. J Hazard Mater 414:125544. https://doi.org/10.1016/j.jhazmat.2021.125544

Chuang CC, Lin CK, Wang TT, Srinivasadesikan V, Raghunath P, Lin MC (2015) Computational and experimental studies on the effect of hydrogenation of Ni-doped TiO$_2$ anatase nanoparticles for the application of water splitting. RSC Adv 5:81371–81377. https://doi.org/10.1039/C5RA16119C

Cinelli G, Cuomo F, Ambrosone L, Colella M, Ceglie A, Venditti F, Lopez F (2017) Photocatalytic degradation of a model textile dye using carbon-doped titanium dioxide and visible light. J Water Process Eng 20:71–77. https://doi.org/10.1016/j.jwpe.2017.09.014

Das N, Madhavan J, Selvi A, Das D (2019) An overview of cephalosporin antibiotics as emerging contaminants: a serious environmental concern. 3 Biotech 9:231. https://doi.org/10.1007/s13205-019-1766-9

Davies KR, Cherif Y, Pazhani GP, Anantharaj S, Azzi H, Terashima C, Fujishima A, Pitchaimuthu S (2021) The upsurge of photocatalysts in antibiotic micropollutants treatment: materials design, recovery, toxicity and bioanalysis. J Photochem Photobiol C: Photochem Rev 48:100437. https://doi.org/10.1016/j.jphotochemrev.2021.100437

Diao Z, Cheng L, Hou X, Rong D, Lu Y, Yue W, Sun D (2019) Fabrication of the hierarchical HZSM-5 membrane with tunable mesoporosity for catalytic cracking of n-dodecane. Catalysts 9:155. https://doi.org/10.3390/catal9020155

Dutta PK, Severance M (2011) Photoelectron transfer in zeolite cages and its relevance to solar energy conversion. J Phys Chem Lett 2:467–476. https://doi.org/10.1021/jz101500z

Easwaramoorthi S, Natarajan P (2009) Characterisation and spectral properties of surface adsorbed phenosafranine dye in zeolite-Y and ZSM-5: photosensitisation of embedded nanoparticles of titanium dioxide. Microporous Mesoporous Mater 117:541–550. https://doi.org/10.1016/j.micromeso.2008.07.042

Elmolla ES, Chaudhuri M (2010) Comparison of different advanced oxidation processes for treatment of antibiotic aqueous solution. Desalin 256:43–47. https://doi.org/10.1016/j.desal.2010.02.019

Guesh K, Márquez-Álvarez C, Chebude Y, Díaz I (2016) Enhanced photocatalytic activity of supported TiO_2 by selective surface modification of zeolite Y. Appl Surf Sci 378:473–478. https://doi.org/10.1016/j.apsusc.2016.04.029

Gurkan YY, Turkten N, Hatipoglu A, Cinar Z (2012) Photocatalytic degradation of cefazolin over N-doped TiO_2 under UV and sunlight irradiation: prediction of the reaction paths via conceptual DFT. Chem Eng J 184:113–124. https://doi.org/10.1016/j.cej.2012.01.011

He Z, Que W, Chen J, He Y, Wang G (2013) Surface chemical analysis on the carbon-doped mesoporous TiO_2 photocatalysts after post-thermal treatment: XPS and FTIR characterization. J Phys Chem Solid 74:924–928. https://doi.org/10.1016/j.jpcs.2013.02.001

Huang M, Xu C, Wu Z, Huang Y, Lin J, Wu J (2008) Photocatalytic discolorization of methyl orange solution by Pt modified TiO_2 loaded on natural zeolite. Dyes Pigm 77:327–334. https://doi.org/10.1016/j.dyepig.2007.01.026

Huang X, Yang W, Zhang G, Yan L, Zhang Y, Jiang A, Xu H, Zhou M, Liu Z, Tang H, Dionysiou DD (2021) Alternative synthesis of nitrogen and carbon co-doped TiO_2 for removing fluoroquinolone antibiotics in water under visible light. Catal Today 361:11–16. https://doi.org/10.1016/j.cattod.2019.10.034

Iskender G, Sezer A, Arslan-Alaton I, Babuna FG, Okay OS (2007) Treatability of cefazolin antibiotic formulation effluent with O_3 and O_3/H_2O_2 processes. Water Sci Technol 55:217–225. https://doi.org/10.2166/wst.2007.325

Jalloul G, Al-Mousawi A, Chocr F, Merhi A, Awala H, Boyadjian C (2022) Fe-sensitized zeolite supported TiO_2 for the degradation of tetracycline using blue LED irradiation. Front Environ Sci 10:873257. https://doi.org/10.3389/fenvs.2022.873257

Jansson I, Suárez S, Garcia-Garcia FJ, Sánchez B (2015) Zeolite-TiO_2 hybrid composites for pollutant degradation in gas phase. Appl Catal Environ 178:100–107. https://doi.org/10.1016/j.apcatb.2014.10.022

Jing Z, Dai X, Xian X, Zhang Q, Zhong H, Li Y (2020) Novel ternary heterogeneous reduction graphene oxide (RGO)/BiOCl/TiO_2 nanocomposites for enhanced adsorption and visible light induced photocatalytic activity toward organic contaminants. Materials 13:2529. https://doi.org/10.3390/ma13112529

Kadi MW, Hameed A, Mohamed RM, Ismail IMI, Alangari Y, Cheng HM (2019) The effect of Pt nanoparticles distribution on the removal of cyanide by TiO_2 coated Al-MCM-41 in blue light exposure. Arab J Chem 12:957–965. https://doi.org/10.1016/j.arabjc.2016.02.001

Li H, Zhang W, Liu Y (2020) HZSM-5 zeolite supported boron-doped TiO_2 for photocatalytic degradation of ofloxacin. J Mater Res Technol 9:2557–2567. https://doi.org/10.1016/j.jmrt.2019.12.086

Liang Y, Guo N, Li L, Li R, Ji G, Gan S (2016) Facile synthesis of Ag/ZnO micro-flowers and their improved ultraviolet and visible light photocatalytic activity. New J Chem 40:1587–1594. https://doi.org/10.1039/C5NJ02388B

Liu M, Zhang L, Xi BD, Yu S, Hu X, Hou LA (2017) Degradation of ciprofloxacin by TiO_2/Fe_2O_3/zeolite catalyst-activated persulfate under visible LED light irradiation. RSC Adv 7:51512–51520. https://doi.org/10.1039/C7RA08475G

Liu X, Liu Y, Lu S, Guo W, Xi B (2018) Performance and mechanism into TiO_2/zeolite composites for sulfadiazine adsorption and photodegradation. Chem Eng J 350:131–147. https://doi.org/10.1016/j.cej.2018.05.141

López-Ortiz A, Pineda IYP, Méndez-Lagunas LL, Ortega AB, Martínez LG, Pérez-Orozco JP, del Río JA, Nair PK (2021) Optical and thermal properties of edible coatings for application in solar drying. Sci Rep 11:10051. https://doi.org/10.1038/s41598-021-88901-5

Mahalingam T, Selvakumar C, Kumar ER, Venkatachalam T (2017) Structural, optical, morphological and thermal properties of TiO_2-Al and TiO_2-Al_2O_3 composite powders by ball milling. Phys Lett A 381:1815–1819. https://doi.org/10.1016/j.physleta.2017.02.053

Mazierski P, Caicedo PNA, Grzyb T, Mikolajczyk A, Roy JK, Wyrzykowska E, Wei Z, Kowalska E, Puzyn T, Zaleska-Medynska A, Nadolna J (2019) Experimental and computational study of Tm-doped TiO_2: the effect of Li^+ on Vis-response photocatalysis and luminescence. Appl Catal Environ 252:138–151. https://doi.org/10.1016/j.apcatb.2019.03.051

Mekki A, Benmaati A, Mokhtar A, Hachemaoui M, Zaoui F, Zahmani HH, Sassi M, Hacini S, Boukoussa B (2020) Michael addition of 1, 3-dicarbonyl derivatives in the presence of zeolite Y as a heterogeneous catalyst. J Inorg Organomet Poly Mater 30:2323–2334. https://doi.org/10.1007/s10904-019-01424-5

Treacy MMJ, Higgins JB (2001) Collection of simulated XRD powder patterns for zeolites. Elsevier

Mutuku C, Gazdag Z, Melegh S (2022) Occurrence of antibiotics and bacterial resistance genes in wastewater: resistance mechanisms and antimicrobial resistance control approaches. World J Microbiol Biotechnol 38:1–27. https://doi.org/10.1007/s11274-022-03334-0

Nagaraj G, Brundha D, Chandraleka C, Arulpriya M, Kowsalya V, Sangavi S, Jayalakshmi R, Tamilarasu S, Murugan R (2020) Facile synthesis of improved anatase TiO_2 nanoparticles for enhanced solar-light driven photocatalyst. SN Appl Sci 2:734. https://doi.org/10.1007/s42452-020-2554-1

Navarra W, Sacco O, Daniel C, Venditto V, Vaiano V, Vignati DAL, Bojic C, Libralato G, Lofrano G, Carotenuto M (2022) Photocatalytic degradation of atrazine by an N-doped TiO_2/polymer composite: catalytic efficiency and toxicity evaluation. J Environ Chem Eng 10:108167. https://doi.org/10.1016/j.jece.2022.108167

Negi C, Kandwal P, Rawat J, Sharma M, Sharma H, Dalapati G, Dwivedi C (2021) Carbon-doped titanium dioxide nanoparticles for visible light driven photocatalytic activity. Appl Surf Sci 554:149553. https://doi.org/10.1016/j.apsusc.2021.149553

Noorjahan M, Kumari VD, Subrahmanyam M, Boule P (2004) A novel and efficient photocatalyst: TiO_2-HZSM-5 combinate thin film. Appl Catal Environ 47:209–213. https://doi.org/10.1016/j.apcatb.2003.08.004

O'regan B, Grätzel M (1991) A low-cost, high-efficiency solar cell based on dye-sensitized colloidal TiO$_2$ films. Nature 353:737–740. https://doi.org/10.1038/353737a0

Oseghe EO, Ofomaja AE (2018) Facile microwave synthesis of pine-cone derived C-doped TiO$_2$ for the photodegradation of tetracy-cline hydrochloride under visible-LED light. J Environ Manage 223:860–867. https://doi.org/10.1016/j.jenvman.2018.07.003

Pandi K, Preeyangghaa M, Vinesh V, Madhavan J, Neppolian B (2022) Complete photocatalytic degradation of tetracycline by carbon doped TiO$_2$ supported with stable metal nitrate hydroxide. Environ Res 207:112188. https://doi.org/10.1016/j.envres.2021.112188

Park J, Back T, Mitchel WC, Kim SS, Elhamri S, Boeckl J, Fairchild SB, Naik R, Voevodin AA (2015) Approach to multifunctional device platform with epitaxial graphene on transition metal oxide. Sci Rep 5:14374. https://doi.org/10.1038/srep14374

Pawar M, Sendoğdular ST, Gouma P (2018) A brief overview of TiO$_2$ photocatalyst for organic dye remediation: case study of reaction mechanisms involved in Ce-TiO$_2$ photocatalysts system. J Nanomater 2018:5953609. https://doi.org/10.1155/2018/5953609

Payra P, Dutta PK (2003) Zeolites: A primer. In: Aubach SM, Carrado KA, Dutta PK (eds) Handbook of zeolites and layered materials. Macel Dekker, Inc., New York, pp 1–24

Polianciuc SI, Gurzău AE, Kiss B, Ştefan MG, Loghin F (2020) Antibiotics in the environment: causes and consequences. Med Pharm Rep 93:231–240. https://doi.org/10.15386/mpr-1742

Rajan MS, John A, Thomas J (2022a) Nanophotocatalysis for the removal of pharmaceutical residues from water bodies: state of art and recent trends. Curr Anal Chem 18:288–308

Rajan MS, Yoon M, Thomas J (2022b) Kaolin-graphene carboxyl incorporated TiO$_2$ as efficient visible light active photocatalyst for the degradation of cefuroxime sodium. Photochem Photobiol Sci 21:509–528. https://doi.org/10.1007/s43630-022-00179-2

Ren W, Ai Z, Jia F, Zhang L, Fan X, Zou Z (2007) Low temperature preparation and visible light photocatalytic activity of mesoporous carbon doped crystalline TiO$_2$. Appl Catal Environ 69:138–144. https://doi.org/10.1016/j.apcatb.2006.06.015

Rossi L, Palacio M, Villabrille PI, Rosso JA (2021) V-doped TiO$_2$ photocatalysts and their application to pollutant degradation. Environ Sci Pollut Res 28:24112–24123. https://doi.org/10.1007/s11356-021-12339-5

Saqib NU, Adnan R, Shah I (2019) Zeolite supported TiO$_2$ with enhanced degradation efficiency for organic dye under household compact fluorescent light. Mater Res Express 6:095506. https://doi.org/10.1088/2053-1591/ab2eb8

Shao J, Sheng W, Wang M, Li S, Chen J, Zhang Y, Cao S (2017) In situ synthesis of carbon-doped TiO$_2$ single-crystal nanorods with a remarkably photocatalytic efficiency. Appl Catal Environ 209:311–319. https://doi.org/10.1016/j.apcatb.2017.03.008

Sharma S, Umar A, Mehta SK, Ibhadon AO, Kansal SK (2018) Solar light driven photocatalytic degradation of levofloxacin using TiO$_2$/carbon-dot nanocomposites. New J Chem 42:7445–7456. https://doi.org/10.1039/C7NJ05118B

Van KN, Huu HT, Thi VNN, Le TLT, Hoang QD, Dinh QV, Vo V, Tran DL, Vasseghian Y (2022) Construction of S-scheme CdS/g-C$_3$N$_4$ nanocomposite with improved visible-light photocatalytic degradation of methylene blue. Environ Res 206:112556. https://doi.org/10.1016/j.envres.2021.112556

Vanichvattanadecha C, Jaroenworaluck A, Henpraserttae P, Wimuktiwan P, Manpetch P, Singhapong W (2021) Ordered mesoporous silica (SBA-16) supporting titania (TiO$_2$) nanoparticles for photodegradation of paraquat (PQ) herbicide. J Porous Mater 28:1137–1153. https://doi.org/10.1007/s10934-021-01065-5

Wang B, Li P, Du C, Wang Y, Gao D, Li S, Zhang L, Wen F (2019) Synergetic effect of dual co-catalysts on the activity of BiVO$_4$ for photocatalytic carbamazepine degradation. RSC Adv 9:41977–41983. https://doi.org/10.1039/C9RA07152K

Wang C, Li Y (2014) Preparation and characterisation of S doped TiO$_2$/natural zeolite with photocatalytic and adsorption activities. Mater Technol 29:204–209. https://doi.org/10.1179/1753555714Y.0000000127

Wang C, Shi H, Li Y (2012) Synthesis and characterization of natural zeolite supported Cr-doped TiO$_2$ photocatalysts. Appl Surf Sci 258:4328–4333. https://doi.org/10.1016/j.apsusc.2011.12.108

Xiao Q, Si Z, Yu Z, Qiu G (2007) Sol-gel auto-combustion synthesis of samarium-doped TiO$_2$ nanoparticles and their photocatalytic activity under visible light irradiation. Mater Sci Eng: B 137:189–194. https://doi.org/10.1016/j.mseb.2006.11.011

Xing M, Li X, Zhang J (2014) Synergistic effect on the visible light activity of Ti^{3+} doped TiO$_2$ nanorods/boron doped graphene composite. Sci Rep 4:5493. https://doi.org/10.1038/srep05493

Xu S, Sun X, Zhao Y, Gao Y, Wang Y, Yue Q, Gao B (2018) Carbon-doped golden wattle-like TiO$_2$ microspheres with excellent visible light photocatalytic activity: simultaneous in-situ carbon doping and single-crystal nanorod self-assembly. Appl Surf Sci 448:78–87. https://doi.org/10.1016/j.apsusc.2018.04.100

Yoon SJ, Lee YH, Cho WJ, Koh IO, Yoon M (2007) Synthesis of TiO$_2$-entrapped EFAL-removed Y-zeolites: novel photocatalyst for decomposition of 2-methylisoborneol. Cat Com 8:1851–1856. https://doi.org/10.1016/j.catcom.2007.02.027

Zhang G, Song A, Duan Y, Zheng S (2018) Enhanced photocatalytic activity of TiO$_2$/zeolite composite for abatement of pollutants. Microporous Mesoporous Mater 255:61–68. https://doi.org/10.1016/j.micromeso.2017.07.028

Zhang L, Ran J, Qiao SZ, Jaroniec M (2019) Characterization of semiconductor photocatalysts. Chem Soc Rev 48:5184–5206. https://doi.org/10.1039/C9CS00172G

Zhang W, Wang K, Yu Y, He H (2010) TiO$_2$/HZSM-5 nanocomposite photocatalyst: HCl treatment of NaZSM-5 promotes photocatalytic degradation of methyl orange. Chem Eng J 163:62–67. https://doi.org/10.1016/j.cej.2010.07.042

Zhao Y, Liang X, Wang Y, Shi H, Liu E, Fan J, Hu X (2018) Degradation and removal of Ceftriaxone sodium in aquatic environment with Bi$_2$WO$_6$/g-C$_3$N$_4$ photocatalyst. J Colloid Interface Sci 523:7–17. https://doi.org/10.1016/j.jcis.2018.03.078

Zhou M, Zhou R, Jiang P, Liang H, Zhou Y, Chen H, Wang B, Chen S, Tu W, Yang Y (2022) Preparation of a novel clay loaded with Fe (VI) for degradation of cefazolin: performance, pathway, and mechanism. Environ Sci Pollut Res 29:46259–46272. https://doi.org/10.1007/s11356-022-18636-x